Geophys. J. Int. (1996) **127**, 49–60

Simulated envelopes of non-isotropically scattered body waves as compared to observed ones: another manifestation of fractal heterogeneity

Alexander A. Gusev[1,2] and Iskander R. Abubakirov[1]

[1] *Institute of Volcanic Geology and Geochemistry, Russian Academy of Sciences, Petropavlovsk-Kamchatsky, Russia*
[2] *Instituto de Geofisica, UNAM, México DF, México*

Accepted 1996 May 16. Received 1996 February 26; in original form 1995 August 11

SUMMARY

Envelopes of scalar waves are simulated at various distances from an instant point source embedded in a random uniformly scattering medium by means of direct Monte-Carlo modelling of wave-energy transport. Three types of scattering radiation pattern ('indicatrix') are studied, for media specified by (1) a Gaussian autocorrelation function of inhomogeneities, (2) a power-law ('fractal', $k^{-\alpha}$) inhomogeneity spectrum and (3) the mix of case (1) and the isotropic indicatrix (very small + large inhomogeneities). We look for a model that can qualitatively reproduce the two most characteristic features of real *S*-wave envelopes of near earthquakes, namely (1) the broadening of the 'direct' wave group with distance and (2) the monotonously decaying shape of the coda envelope that does not deviate strongly from that expected in the isotropic scattering case. Both properties are observed for any band over a wide frequency range (1–40 Hz). The well-studied isotropic scattering model realistically predicts the appearance of codas but fails to predict pulse broadening. The model of large-scale inhomogeneity realistically predicts the mode of pulse broadening but fails to predict codas. We have found that, for a particular frequency band, within each class of inhomogeneity studied, both requirements can be qualitatively satisfied by a certain choice of parameters. In the Gaussian-ACF case, however, this match can be obtained only for a narrow frequency range. In contrast, the fractal case (with a value of exponent α of about 3.5–4) reproduces qualitatively the observed wide-band behaviour, and we consider it a reasonable representation of the gross properties of the earth medium.

Key words: fractals, Monte-Carlo simulation, scattering, seismic waves.

INTRODUCTION

Following the work of Aki (1969) and Aki & Chouet (1975), the idea of considering the coda of a local earthquake as the product of scattering of the initial short body-wave pulse in a random medium has become widely accepted. It is less common, however, to consider the entire record of a near earthquake, including both the 'direct' wave group and the coda, in such a manner. Some steps in this direction were taken by Sato (1977, 1984, 1989), Gusev & Abubakirov (1987) and Zeng, Su & Aki (1991). Although these papers dealt with both 'direct' waves and coda, they did not provide an efficient method of interpretation of the entire record in terms of the parameters of the scattering medium. Better methods, based on the integration of a squared record over time, were first proposed by Wu (1985) and Hoshiba (1993). It was assumed in most of the cited studies that the scattering radiation pattern or directivity function ('indicatrix') is isotropic (spherically symmetrical), and in many cases it was shown that real data can be fitted rather well by theoretical trends based on such an isotropic scattering model. Physically, the isotropic scattering model is associated with an inhomogeneity size much less than that of the wavelength.

Another approach, based on the observation of the broadening of a 'direct' wave power pulse, i.e. a non-coherent *S*-wave group, with distance and assuming forward scattering (that is, a forward-enhanced scattering indicatrix), was used by Gusev & Lemzikov (1983, 1985), in which a quadratic trend of the pulse width versus the distance was proposed, and the first estimates of the mean free path were carried out. Further improvements were made by Abubakirov & Gusev (1990) who used two techniques, both based on the energy transport approach: an analytical (multiple low-angle scattering) technique and a numerical (Monte-Carlo) technique. A detailed

study of pulse broadening was carried out by Sato (1989) and Scherbaum & Sato (1991) based on the parabolic approximation (PA) for a plane wave, assuming that the inhomogeneity size is much larger than that of the wavelength. Both studies compared their respective theories with real data. Theoretical trends matched the observed ones reasonably well. Finally, Gusev & Abubakirov (1987) and Hoshiba (1995) tried to use non-isotropic, multiple, forward-scattering models to fit the parameters of observed envelopes—an approach that can combine the positive aspects of both presented approaches.

To do this effectively, one must resolve a puzzling contradiction that reveals itself when one notices that the theories that have been successfully applied to real data assume two radically different model indicatrices: (1) isotropic, in order to predict the coda decay shape, and (2) non-isotropic, strongly forward-enhanced, in order to describe pulse broadening. It was shown by Gusev & Abubakirov (1987) that at distances that are small compared to the mean free path even a moderately narrow (20°) indicatrix leads to an unrealistically fast decay of the coda envelope just after the direct wave group. A qualitatively similar fast decay is predicted by the PA theory. The question arises whether it is possible to find indicatrix functions that can simultaneously produce both realistic coda shapes and realistic pulse broadening. In the following we try to answer this question. As candidate models, we will study a model with a single well-defined characteristic size, specifically a model with a Gaussian autocorrelation function of inhomogeneities, and a multiple-scale model, with a power-law inhomogeneity spectrum, which describes fractal inhomogeneity, proposed explicitly for the lithosphere by Wu & Aki (1985b).

To obtain theoretical envelopes of scattered waves we use the numerical Monte-Carlo approach. Our earlier technique (Gusev & Abubakirov 1987) will be applied with some important modifications.

GENERAL THEORETICAL BACKGROUND

In this section we will briefly present some known results that form the basis of our technique. Refer to Ishimaru (1978), Rytov *et al.* (1978) for general and Wu (1985), Sato (1995) for seismologically oriented presentations of the underlying theory. Let us specify the random/incoherent scalar wavefield by its (radiation) intensity, $I_s(\mathbf{r}, \mathbf{n})$, defined by the relation

$$dI_s = I_s(\mathbf{r}, \mathbf{n})\, d\Omega_n\,, \tag{1}$$

where dI_s is the radiation energy flux into a solid angle $d\Omega_n$ with its vertex at a location $\mathbf{r}$ and its direction along a unit vector $\mathbf{n}$. The difference in intensity values at two adjacent points on the same ray $\mathbf{n}$ separated by the distance dl can be represented as a sum of two terms representing loss and gain:

$$I_s(\mathbf{r} + \mathbf{n}\, dl, \mathbf{n}) - I_s(\mathbf{r}, \mathbf{n}) = -dI_1 + dI_2\,. \tag{2}$$

Loss can be represented as a sum of the scattering loss and the intrinsic (absorption) loss:

$$dI_1 = I_s(\mathbf{r}, \mathbf{n})\alpha_s dl + I_s(\mathbf{r}, \mathbf{n})\alpha_i\, dl\,, \tag{3}$$

where α_s and α_i are the scattering and absorption coefficients [$l_n = 1/\alpha_s$ is referred to as the (non-isotropic) mean free path (MFP)]. Gain is produced by scattering from all other propagation directions into $\mathbf{n}$:

$$dI_2 = \int_{4\pi} I_s(\mathbf{r}, \mathbf{m}) f(\mathbf{n}, \mathbf{m})\, d\Omega_m\, dl\,, \tag{4}$$

where $f(\mathbf{m}, \mathbf{n})$ is the differential scattering coefficient, or the differential cross-section of unit volume of the medium, describing wave intensity transfer from a direction $\mathbf{m}$ into a direction $\mathbf{n}$. (4) can be thought of as a definition for $f(\mathbf{m}, \mathbf{n})$. From (2), for the derivative along $\mathbf{n}$ we now obtain

$$\frac{dI_s(\mathbf{r}, \mathbf{n})}{dl} = (\alpha_s + \alpha_i) I_s(\mathbf{r}, \mathbf{n}) + \int_{4\pi} I_s(\mathbf{r}, \mathbf{m}) f(\mathbf{m}, \mathbf{n})\, d\Omega_m\,. \tag{5}$$

This is the basic equation of the radiative transfer theory, valid when the mean/coherent field is zero, that is, far from the sources of waves. To account also for the mean field, one more equation of a similar structure must be added to form a system

$$\begin{cases} \dfrac{dI_s(\mathbf{r}, \mathbf{n})}{dl} = -(\alpha_s + \alpha_i) I_s(\mathbf{r}, \mathbf{n}) \\ \qquad\qquad + \displaystyle\int_{4\pi} [I_s(\mathbf{r}, \mathbf{m}) + I_0(\mathbf{r}, \mathbf{m})] f(\mathbf{m}, \mathbf{n})\, d\Omega_m\,, \\ \dfrac{dI_0(\mathbf{r}, \mathbf{n})}{dl} = -(\alpha_s + \alpha_i) I_0(\mathbf{r}, \mathbf{n})\,, \end{cases} \tag{6}$$

where $I_0(\mathbf{r}, \mathbf{n})$ is the radiation intensity of the mean field. The loss term is present for the mean/coherent field but the gain term is not, because coherency cannot be restored and a random field cannot produce a coherent one (i.e. one with a non-zero mean). Adding both equations, the equation for the total intensity, $I = I_0 + I_s$, which is similar to (5), is obtained:

$$\frac{dI(\mathbf{r}, \mathbf{n})}{dl} = -(\alpha_s + \alpha_i) I(\mathbf{r}, \mathbf{n}) + \int_{4\pi} I(\mathbf{r}, \mathbf{m}) f(\mathbf{m}, \mathbf{n})\, d\Omega_m\,. \tag{7}$$

This is the basic equation for our modelling. As one would expect, α_s is related to $f(\mathbf{m}, \mathbf{n})$:

$$\alpha_s = \int_{4\pi} f(\mathbf{m}, \mathbf{n})\, d\Omega_m \left(= \int_{4\pi} f(\mathbf{m}, \mathbf{n})\, d\Omega_n \right), \tag{8}$$

i.e. the entire scattering loss for a direction $\mathbf{n}$ is the sum of the losses into each of the other directions. Dividing $f(\mathbf{m}, \mathbf{n})$ by α_s, a normalized scattering radiation pattern, or 'indicatrix' function [following the usage of optics, see e.g. Rytov *et al.* (1978)], is obtained:

$$\phi_0(\mathbf{m}, \mathbf{n}) = f(\mathbf{m}, \mathbf{n})/\alpha_s\,, \qquad \int_{4\pi} \phi_0(\mathbf{m}, \mathbf{n})\, d\Omega_n = 1\,. \tag{9}$$

Radiative transfer theory was initially developed on a phenomenological basis. Later, it was related to wave-propagation theory. The radiative transfer equation can be derived from the Bethe–Salpeter equation for a two-point coherence function of a multiple-scattered random wavefield with some fairly unrestrictive additional conditions (Rytov *et al.* 1978). One is that the wavelength must be small compared to the non-isotropic mean free path $1/\alpha_s$, which is merely the assumption of weak scattering. Another is that

$$(ka)^2 \sigma_\varepsilon^2 \ll 1\,, \tag{10}$$

where k is the wavenumber, a is the correlation radius of the inhomogeneity field, and σ_ε^2 is the mean square fractional velocity fluctuation, usually much below unity. The case of

very large ka is not covered by this condition, but it can still be treated on the basis of the radiation transfer equation if the parabolic equation approximation is applicable. Therefore, the domain of formal correspondence between the full-wave approach and the radiative-transfer approach is rather wide. (This does not mean that the radiative-transfer approach will necessarily produce errors outside this domain: in many cases the field of applicability of an approximate method in the wave-scattering theory is much wider than could be expected on the basis of a formal analysis.)

The relationship of the differential-scattering coefficient $f(\mathbf{m}, \mathbf{n})$ with the properties of the medium is as follows (Ishimaru 1978). For a random weakly scattering acoustic medium, $f(\mathbf{m}, \mathbf{n})$ can be expressed through the autocorrelation function (ACF) of the inhomogeneity field. Let this field be specified by the fractional velocity fluctuation $\varepsilon(\mathbf{r})$. Its ACF is then defined as

$$C_0(\mathbf{s}) = \langle \varepsilon(\mathbf{r})\varepsilon(\mathbf{r}+\mathbf{s}) \rangle \tag{11}$$

(here $C_0(\mathbf{s})$ is assumed to be the same for any $\mathbf{r}$, i.e. the inhomogeneity field is assumed to be statistically uniform). The Fourier transform of $C_0(\mathbf{s})$ gives the power spectral density of inhomogeneity,

$$\tilde{C}_0(\mathbf{k}) = \int C_0(\mathbf{s}) \exp(-i\mathbf{ks})\, d^3\mathbf{s}\,. \tag{12}$$

For the isotropic inhomogeneity fields considered below, $C_0(\mathbf{s}) = C(s)$ and $\tilde{C}_0(\mathbf{k}) = \tilde{C}(k)$. Then, $f(\mathbf{m}, \mathbf{n})$ is determined by

$$f(\mathbf{m}, \mathbf{n}) = 2\pi k^4 \tilde{C}_0[k(\mathbf{m}-\mathbf{n})] = 2\pi k^4 \tilde{C}[2k \sin(\theta/2)]\,, \tag{13}$$

where $\theta = \cos^{-1}(\mathbf{mn})$ is the scattering (deflection) angle. Note that this is true for weak scattering only, i.e. in the Born approximation.

PRINCIPLES OF THE NUMERICAL MODELLING: THE CHOICE OF SCALING

In the following we apply the Monte-Carlo technique to study the wave energy propagation through a random medium. This approach is a standard one for solution of the radiation transfer equation in atmospheric optics or of its analogue in neutron transport theory. Although practically all problems considered in these fields are stationary, the direct Monte-Carlo approach, when particles or ray propagation trajectories are traced in model time, needs no significant modification to deal with non-stationary problems. Note that (6) does not contain a time variable. A general formulation of the non-stationary radiation transfer problem was recently proposed by Sato (1995).

Let us consider the relation between radiation transfer equation (6) and the Monte-Carlo modelling procedure. Rewrite (6) explicitly expressing scattering loss into each direction:

$$\frac{dI(\mathbf{r}, \mathbf{n})}{dl} = -I(\mathbf{r}, \mathbf{n}) \int_{4\pi} f(\mathbf{n}, \mathbf{m})\, d\Omega_{\mathrm{m}} - \alpha_{\mathrm{i}} I(\mathbf{r}, \mathbf{n}) + \int_{4\pi} I(\mathbf{r}, \mathbf{m}) f(\mathbf{m}, \mathbf{n})\, d\Omega_{\mathrm{m}}\,. \tag{14}$$

We will model the $I(\mathbf{r}, \mathbf{n})$ function by particle density $N(\mathbf{r}, \mathbf{n})$. Particles are thought to be propagating along their trajectories/rays with a constant velocity c. For a finite small spatial increment Δl, with some manipulation one obtains

$$\frac{\Delta N(\mathbf{r}, \mathbf{n})}{N(\mathbf{r}, \mathbf{n})} = -\alpha_{\mathrm{s}} \Delta l \int_{4\pi} \phi_0(\mathbf{n}, \mathbf{m})\, d\Omega_{\mathrm{m}} - \alpha_{\mathrm{i}} \Delta l + \frac{\alpha_{\mathrm{s}} \Delta l}{N(\mathbf{r}, \mathbf{n})} \int_{4\pi} \phi_0(\mathbf{m}, \mathbf{n}) N(\mathbf{r}, \mathbf{m})\, d\Omega_{\mathrm{m}}\,. \tag{15}$$

The left side of this relation is the fractional change of the number of particles moving in the $\mathbf{n}$ direction on a path element Δl. It consists of three terms, representing a fraction that leaves direction $\mathbf{n}$, a fraction that dies off, and a term representing gain produced by scattering from each of the other directions into $\mathbf{n}$. When a modelled particle propagates over Δl, only the first two terms need to be modelled; the third will be modelled automatically when propagation along other directions are modelled in their (random) turn. Thus, a particle propagating over an elementary path Δl is either scattered with the probability $\alpha_{\mathrm{s}} \Delta l$, or disappears with the probability $\alpha_{\mathrm{i}} \Delta l$, (or continues its motion along $\mathbf{n}$, with the probability $[1 - (\alpha_{\mathrm{s}} + \alpha_{\mathrm{i}})\Delta l]$). If it is scattered, it 'chooses' a new direction with the probability $\Pr(\mathbf{m}) = \phi_0(\mathbf{n}, \mathbf{m})$. Note that $\phi_0(\mathbf{n}, \mathbf{m})$ was accordingly normalized in advance.

In this paper we study the simple case of an instant point-radiation source with an isotropic radiation pattern; intrinsic loss will not be accounted for ($\alpha_{\mathrm{i}} = 0$). The source is located at $\mathbf{r} = 0$ and produces a pulse at $t = 0$. Integrating source radiation intensity $I_0(\mathbf{r}, \mathbf{n}) = N_0(\mathbf{r}, \mathbf{n}) \approx N(\mathbf{r}, \mathbf{n})$ over a small sphere of radius R, centred on the source, one obtains the source energy

$$M = 4\pi R^2 N_0(0, \mathbf{n})\,. \tag{16}$$

If $M = 1$, the resulting radiation field $N(\mathbf{r}, \mathbf{n})$ is essentially the Green's function of the radiation transfer problem. We will use the condition $M = 1$ throughout this paper. Although the temporal evolution of $N(\mathbf{r}, \mathbf{n})$ has not been expressed explicitly yet, it is generally time-dependent. With the Monte-Carlo technique, the temporal evolution is modelled automatically due to the emission of particles at a specified moment and their propagation with a definite velocity. We do not accumulate the directional information during modelling, so only the (omnidirectional) energy density,

$$e(\mathbf{r}, t) = (1/M) \int_{4\pi} N(\mathbf{r}, \mathbf{n}, t)\, d\Omega_{\mathrm{n}}\,, \tag{17}$$

will be discussed further.

An important property of the scattering radiation field is its asymptotic behaviour at large t. Following Ishimaru (1978) we shall assume that at large t, $e(\mathbf{r}, t)$ obeys the diffusion equation (Wesley 1965; Aki & Chouet 1975), with the diffusion coefficient $D = l_{\mathrm{e}}/3$, where l_{e} is the effective mean free path. Thus one cannot distinguish between various indicatrix functions if $e(\mathbf{r}, t)$, or even $N(\mathbf{r}, \mathbf{n}, t)$, is known for large t only. The relationship between l_{e} and $l_{\mathrm{n}} = 1/\alpha_{\mathrm{s}}$ is given by

$$l_{\mathrm{e}} = l_{\mathrm{n}}(1 - \langle \cos\theta \rangle)^{-1}\,, \qquad \langle \cos\theta \rangle = \int_{4\pi} \cos\theta \phi_0(\mathbf{n}, \mathbf{m})\, d\Omega_{\mathrm{m}} \tag{18}$$

(Ishimaru 1978). Therefore, if $\phi_0(\mathbf{m}, \mathbf{n}) = \mathrm{const} = 1/4\pi$, $l_{\mathrm{e}} = l_{\mathrm{n}}$. This isotropic scattering case has been much studied (see e.g. Zeng *et al.* 1991 and references therein); it can be considered as a natural reference for more complicated cases. If we associate earthquake coda with the described asymptotic case, then MFP values determined based on the coda level will

represent l_e, and do not provide any direct information about l_n. We will show below that l_e is the characteristic distance determining, in addition to coda level, scattering effects such as pulse broadening.

To simplify the theoretical analysis, we performed our modelling in dimensionless variables. To do this, we set l_e and c to unity. To relate the results with the real data, one should normalize real distance and real time by the values of effective MFP l_e and 'effective mean free time' $t_* = l_e/c$. We denote the normalized coordinate vector, hypocentral distance and time as $\bar{\rho}$, ρ and τ respectively. Note that with $c = 1$, wave-energy density is equal to wave-energy flux. Hence, we can treat the square root of particle density as the wave amplitude, and it is this quantity that will be presented in the figures that follow. In ρ–τ coordinates, large-τ asymptotics of all envelope functions (late codas) must (and will) coincide, enabling their easy comparison at earlier times (and, incidentally, a check of the Monte-Carlo numerical scheme).

THE MODELLING PROCEDURE

The Monte-Carlo modelling scheme of Gusev & Abubakirov (1987) was employed with some important improvements. As only the spherically symmetrical case is treated, we determine the function

$$i(\rho, \tau) = e(\rho, \tau)|_{|\rho| = \rho} \tag{19}$$

directly. Recall that this is the volume particle density normalized to one radiated particle ($M = 1$). To estimate $i(\rho, \tau)$ at each particular τ, we count particles in each bin of the size $\Delta\rho$ around ρ and then divide the result by the bin volume and by the total particle number. Each modelled particle is emitted from the point source at $\rho = 0$, $\tau = 0$ in a spherically symmetrical manner (this is in fact excessive: any radiation pattern would do). Then, its 3-D trajectory is 'monitored' during all the specified modelling time. A trajectory consists of discrete unit substeps of fixed length $L \ll l_n$. The number of substeps constituting any particular linear segment of a trajectory (i.e. 'free path') is drawn out of the geometric distribution, chosen so that the average free path is equal to l_n. This technique is a discrete analogue of the standard exponential distribution of the free path, with the probability density $p(x) = \exp(-x/l_n)l_n$. For each scattering event, we must determine two angles that define the direction of the next free path relative to the current one. One of them is the scattering angle θ, and it is modelled by drawing a random number according to the particular indicatrix. We also need a second angle ('longitude', if θ is thought of as polar distance on a unit sphere). As we are working here with axisymmetrical indicatrices, this angle is modelled as a uniform random over $(0, 2\pi)$. Each trajectory is completely independent of any other. Particle position is recorded with a constant pre-determined time step, which is equal to or is a natural multiple of L, thus avoiding the accumulation of a rounding error. The number of traced particles varied typically between 20 000 and 100 000. The number of distance bins was 50, and the number of time steps, 200–1000. Thus, the typical temporal resolution of model envelopes was about 1 per cent of the traveltime. Wide ranges of time/distance were covered by a series of simulations, each with a different bin size and time step.

Two particular classes of indicatrix functions can be chosen for modelling: 'Gaussian ACF' and 'fractal'. Both describe the scalar wave scattering in a medium with an isotropic random inhomogeneity field of a particular kind. For versatility, any indicatrix can, in addition, be mixed with an isotropic (constant over a unit sphere) indicatrix in any proportion. In the Gaussian-ACF case, the autocorrelation function (ACF) and power spectrum of inhomogeneity are

$$C(r) = \sigma_\varepsilon^2 \exp(-r^2/a^2), \qquad \tilde{C}(k) = \pi^{3/2} a^3 \sigma_\varepsilon^2 \exp(-(ka)^2/4), \tag{20}$$

where $\sigma_\varepsilon^2 = C(0) = \langle \varepsilon(r)\varepsilon(r) \rangle$, and a ('correlation radius') specifies the characteristic scale of inhomogeneity. This gives the indicatrix function [which we redefine here as a function of the angle θ so that $\phi(\theta) = \phi(\arccos(\mathbf{mn})) = \phi_0(\mathbf{m}, \mathbf{n})$] and $\langle \cos\theta \rangle$ as

$$\phi(\theta) = \frac{\exp((\cos\theta - 1)/\sigma^2)}{2\pi\sigma^2(1 - \exp(-2/\sigma^2))}, \quad \langle \cos\theta \rangle = \frac{1 + \exp(-2/\sigma^2)}{1 - \exp(-2/\sigma^2)} - \sigma^2, \tag{21}$$

where $\sigma = 2^{1/2}/ka$. Note that at large ka, the usual case, the indicatrix becomes a narrow axisymmetrical lobe around the initial direction. As this takes place, $\phi_0(\mathbf{m}, \mathbf{n})$ approaches the 2-D Gaussian probability density over Ω. We introduce a locally orthogonal coordinate system on the unit sphere, with its origin corresponding to the initial direction $\mathbf{m}$, and two angular coordinates δ_1 and δ_2. For small θ the indicatrix function $\phi(\theta)$ converges to the Rayleigh distribution density over θ, which corresponds to a 2-D Gaussian bell over δ_1 and δ_2 with a standard deviation σ over each of these coordinates. Hereafter we will therefore treat σ as an angular quantity. The case when the indicatrix function as such makes a 2-D Gaussian bell over two angular coordinates has been studied previously (Gusev & Abubakirov 1987; Abubakirov & Gusev 1990). It should not be confused with the 'Gaussian-ACF' case. These two cases are, however, practically identical if $\sigma < 20°$.

The 'fractal' case, i.e. scattering by a random inhomogeneity field with a power-low spectrum, was modelled essentially in the same manner. A simple power law, however, produces an indicatrix that is, in general, non-integrable at small θ. To overcome this problem, we assume a low-wavelength cutoff ('fractal limit') of the fluctuation spectrum at $k = k_0$. The corresponding indicatrix is

$$\tilde{C}(k) \propto \begin{cases} 1, & k < k_0 \\ (k/k_0)^{-\alpha}, & k > k_0 \end{cases}, \qquad \phi(\theta) \propto \begin{cases} (\sin\theta_0/2)^{-\alpha}, & 0 < \theta < \theta_0 \\ (\sin\theta/2)^{-\alpha}, & \theta_0 < \theta < \pi \end{cases}. \tag{22}$$

Note that the case $\alpha = 0$ corresponds to isotropic scattering, $\alpha = 3$ is the self-similar fractal case, and the case $\alpha = 4$ is near to that of the exponential autocorrelation function with a correlation radius $a \approx 1/k\theta_0$.

To realize probability distributions representing indicatrices (21) and (22), corresponding random-number generators were designed. They use σ or (θ_0, α) as the parameters. To relate l_n to $l_e \equiv 1$, the values of $\langle \cos\theta \rangle$ were calculated by analytical integration for the Gaussian-ACF case and by numerical integration for other cases. Also, each modelling run gives, as a by-product, a Monte-Carlo integration estimate of $\langle \cos\theta \rangle$ providing an inner check of the procedure.

To illustrate the modelling procedure and at the same time to obtain some insight into the studied phenomena, we created some illustrations, which, for the sake of graphical clarity, were calculated for the 2-D medium and for the needle-like source-radiation pattern. Fig. 1 shows the appearance of trajectories

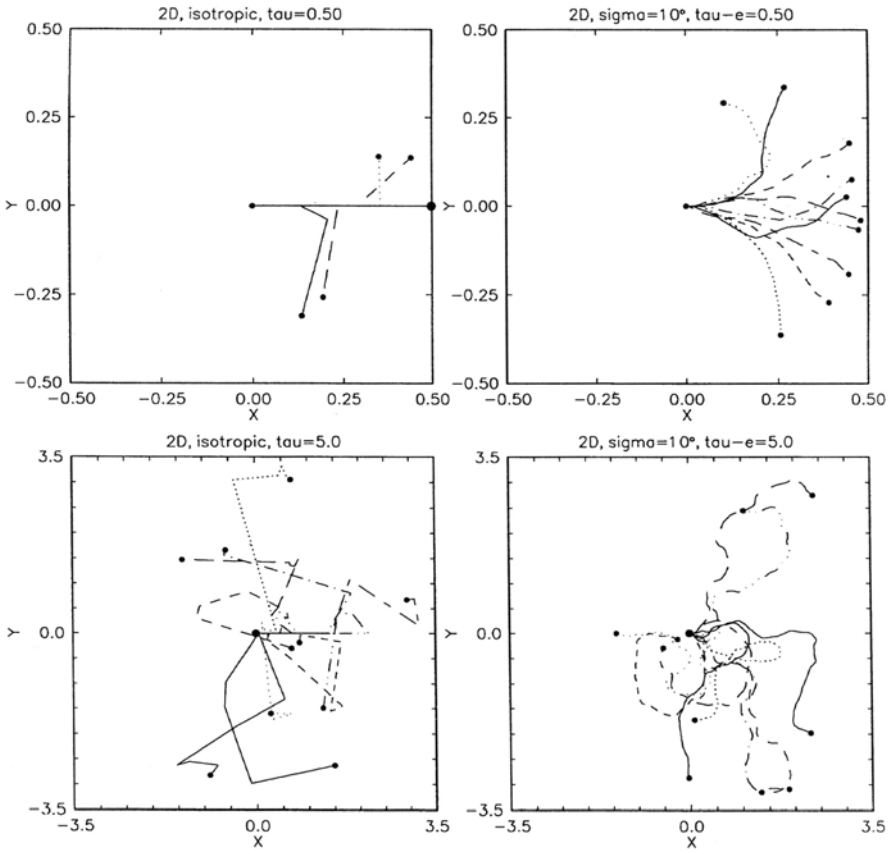

Figure 1. 10 random 2-D trajectories traced up to dimensionless time $\tau = 0.5$ (upper row) and 5.0 (lower row), simulated with two model indicatrices: isotropic (left column) and Gaussian ACF with $\sigma = 10°$ (right column). X and Y are the components of the dimensionless 2-D position vector $\bar{\rho}$. The black dot at (0.5, 0.0) on the top left graph denotes six unscattered particles.

for the cases of isotropic and strongly non-isotropic indicatrices. At $\tau = 0.5$, about half of the isotropically scattered particles propagate 'coherently', producing the delta-like peak; the rest are moving along angular paths. As $l_e/l_n \approx 33$, no 'coherent' non-isotropically scattered particles are left at $\tau = 0.5$: all are moving along visually smooth trajectories. One can see from this figure that energy loss by scattering by large angles from the initial ray is indeed described by l_e and not by l_n. At large $\tau(= 5.0)$, for both indicatrices one observes the feature of the diffusion regime: the coherent component is absent even in the isotropic case, the initial direction of propagation is completely forgotten, and the average distance from the origin is of the order of $\tau^{0.5} \approx 2.3$, as it should be for diffusion.

Fig. 2 shows only the final particle positions for 500 particles at $\tau = 0.7$. In addition to the delta-like direct pulse noted above, which is present in the isotropic case and absent in the non-isotropic one, we see here two more subtle differences between these cases. First, in the non-isotropic case the particles mostly fill a finite layer adjacent to the (circular) wavefront, so that the energy arrival broadens, and one can expect a finite duration of the 'direct' wave pulse, instead of the delta-like pulse in the isotropic case. Second, the neighbourhood of the source is practically free of illumination in the non-isotropic case, whereas in the isotropic case the particles fill the interior of the wavefront more or less homogeneously. This means that for $\sigma = 10°$ only a very weak coda is expected immediately after the direct-wave arrival at a receiver located near enough to the source. The cause of this is that particles/rays are not permitted to turn by large angles, and to make a full turn they must propagate as far/long as $\tau = 1$.

To demonstrate these properties graphically, we calculated the $e(\rho, \tau)$ function for three indicatrices: isotropic, and two Gaussian-ACF ones, with $\sigma = 35°$ and $10°$ (Fig. 3). As already noted, we consider it appropriate to express all our results in terms of amplitude, not power; thus instead of $e(\rho, \tau)$, we plot, here and below, the 'amplitude' function, defined merely as $[e(\rho, \tau)]^{1/2}$, and denote it as A on the plot. In the case $\sigma = 10°$, one can see the deep minimum of amplitude, which, at small distances ($\rho < 0.4$), begins just after the direct arrival and extends up to $\tau \approx 0.5$. The shape of the 'direct pulse' is, however, quite realistic, with the duration quickly increasing with distance. In the isotropic scattering case, the coda decay is (realistically) monotonous, even at small ρ, but the direct wave is always delta-like. The case of $\sigma = 35°$ presents some more or less acceptable compromise between these cases. In the following we will discuss this situation in detail for the 3-D case.

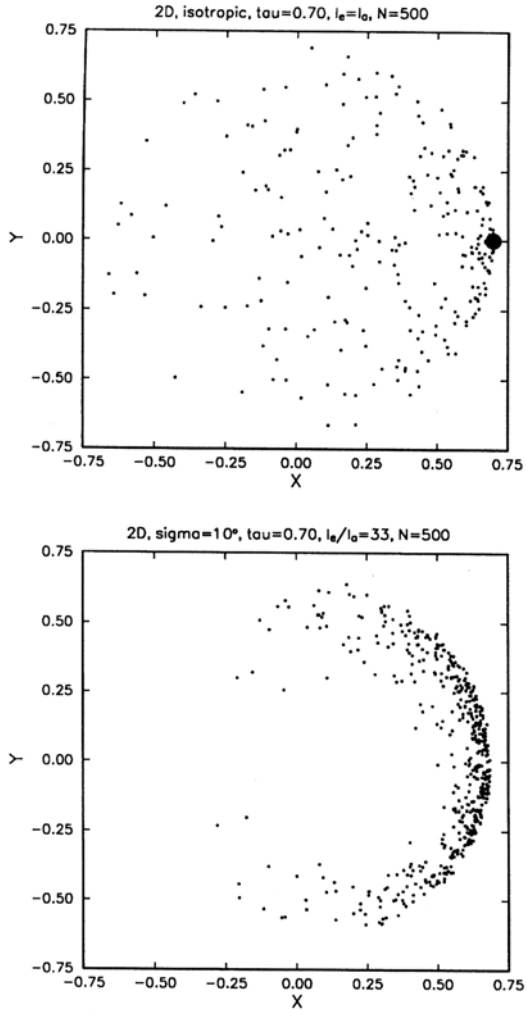

Figure 2. Positions of 500 model particles at $\tau = 0.7$ for two model indicatrices (see Fig. 1). The black dot denotes about 250 unscattered particles.

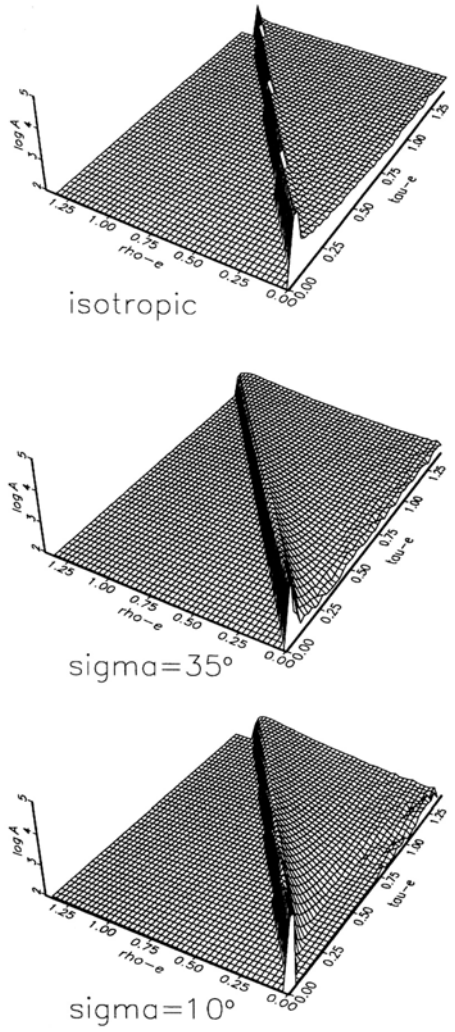

Figure 3. The envelopes $e(\rho, \tau)$ for 2-D scattering with three different indicatrices, simulated with 10^5 particles. Left axis is ρ, right axis is τ. Space-time evolution is presented: at any fixed ρ, a record envelope can be seen, and at any fixed τ, a snapshot of spatial energy distribution can be seen. The 'pool' at the right plot at $\tau = 0.1$–1.07 and $\rho = 0$–0.1 is in fact deeper, but unmeasurable with the actual accuracy; thus an arbitrary 'waterlevel' is introduced. Simulation noise is visible as ripples at small ρ and small amplitudes.

RESULTS OF THE MODELLING

Gaussian-ACF indicatrix

We start with the Gaussian-ACF case as the simplest one. In Fig. 4 one can see the evolution of the scattered amplitude envelope with distance for $\sigma = 6°$, 20°, 40° and 60° ($ka = 13.4$, 4.05, 2.03 and 1.35). The isotropic case ($\sigma = \infty$, $ka = 0$) is also shown. Each plot was obtained in a series of three simulations, with τ-step values of 0.0001, 0.04 and 0.2. For reference, the asymptotic ($\rho = 0$, coda) isotropic envelope shape (Eq. 45 of Abubakirov & Gusev 1990) is drawn on all plots. Because of the very large dynamic range, the lower parts of some modelled curves are noisy and are not drawn. To relate these and the following plots to reality, one can crudely let $l = 50$–100 km, so that $\rho = 1$ can be read as $r = 70$ km. For the most interesting range, $\rho = 0.1$–2, more detailed results are given in the lower right box of Fig. 4 for $\sigma = 6°$. One can see that the asymptotic coda curve still exists, even in this not very realistic case, but its shape radically differs from any observed one. For $\sigma = 20°$, the deviation from the isotropic case is smaller, but still more than one order of magnitude, whereas at $\sigma = 60°$ an unrealistic δ-like pulse is seen, like in the isotropic case. Therefore, only the indicatrices with $\sigma = 30$–$40°$ can produce more or less realistic envelopes, confirming the earlier conclusions of Gusev & Abubakirov (1987) based on the very limited simulation experience.

In Fig. 5, drawn on a natural scale, several 'direct-wave' pulses are shown, for small and medium ρ. For $\sigma = 3°$ the

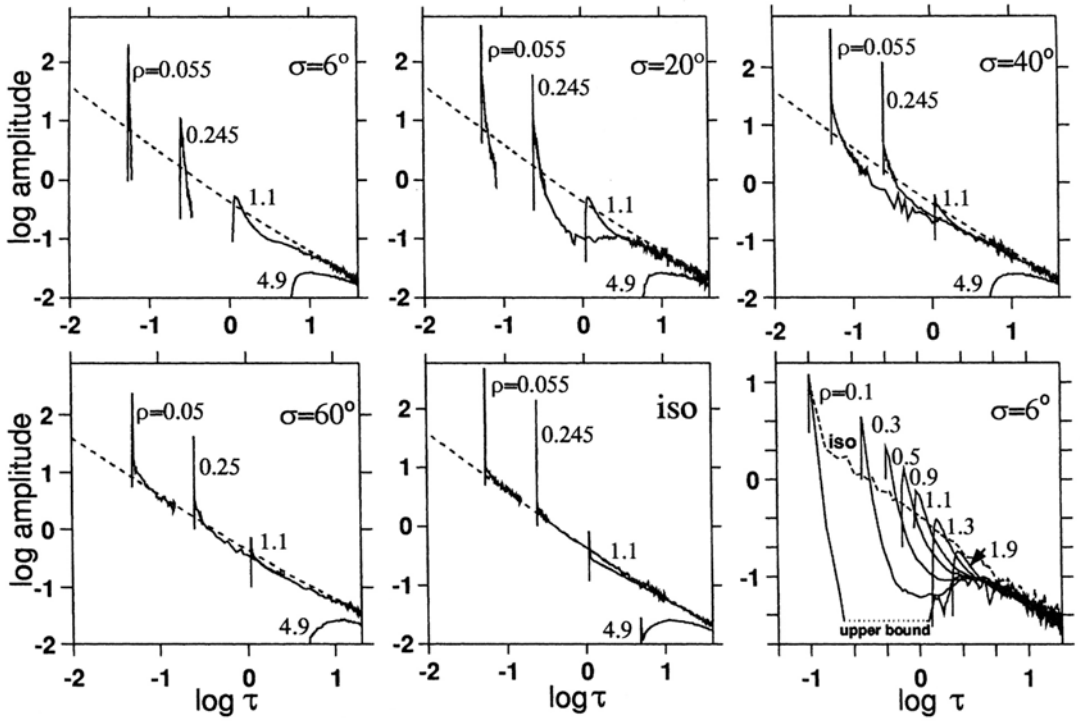

Figure 4. The families of scattered envelopes in the 3-D Gaussian-ACF case, for various values of the indicatrix width parameter σ (first four graphs), and for the isotropic case. On all five plots, the asymptotic coda shape for the isotropic case is shown by dashes. The last graph shows the central part of the first one in detail.

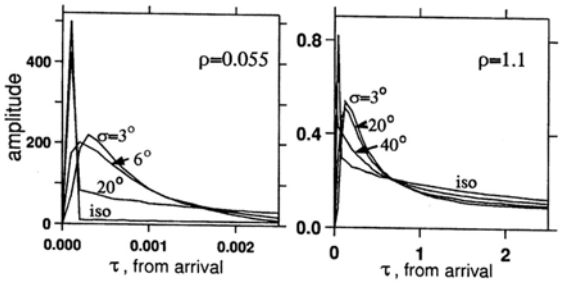

Figure 5. The near-onset part of 3-D Gaussian-ACF envelopes on the natural scale for two values of distance for various σ values, and for the isotropic case for two values of distance. τ steps are 0.0001 (left plot) and 0.0025 (right plot). The inequality of visible envelope areas would disappear if we plotted power instead of amplitude.

'direct-wave' pulse with a lagged maximum can already be seen at $\rho = 0.055$, but is not yet formed for $\sigma = 20°$ at this distance: a sawtooth pulse with an abrupt leading edge, combined with the genuine δ-like direct-wave pulse, is seen. At $\rho = 1.1$, pulse shapes are almost similar for both of these σ values. The change from the abrupt to the smooth leading edge takes place at $\rho \approx 0.05$ for $\sigma = 6°$, at $\rho \approx 0.1$ for $\sigma = 10°$, at $\rho \approx 0.25$ for $\sigma = 20°$ and at $\rho \approx 2$ for $\sigma = 40°$. An important qualitative result is that after this change, the pulse shape at any given σ converges to a certain asymptotic shape that is independent of σ. This observation is evidently related to the concept of 'saturated fluctuations' (see Sato 1989): after some evolution, the pulse shape expected from parabolic approximation must stabilize at some distance and at greater distances follow a definite asymptotic shape function (i.e. the pulse shape becomes identical after the corresponding time axis expansion/compression). This also could be expected from the numerical (Monte-Carlo) and analytical analyses of Williamson (1972). It is shown there that the formation of a standard asymptotic pulse shape is related simply to the multiplicity of scattering: when the number of scattering events becomes large, an asymptotic shape arises. Its analytic expression is cited later.

One can see in Fig. 5 that, for a given distance, the asymptotic pulses coincide for various σ. (This coincidence is specific for our scaling, i.e. for the particular choice of dimensionless variables τ and ρ.) This fact suggests that the characteristic pulse duration depends only on the scaled distance and does not depend on σ, provided that it is small enough. This is just what could be expected based on the results of Williamson (1972, 1975) as well as on the simple theory of multiple low-angle scattering presented in Abubakirov & Gusev (1990). It is this property that gives one the possibility of estimating l_e from the duration versus distance data.

'Fractal' indicatrix

As an alternative to the Gaussian-ACF case with a single characteristic size of inhomogeneity, we also studied multiscale cases, starting with the fractal one. Fig. 6 shows our results for

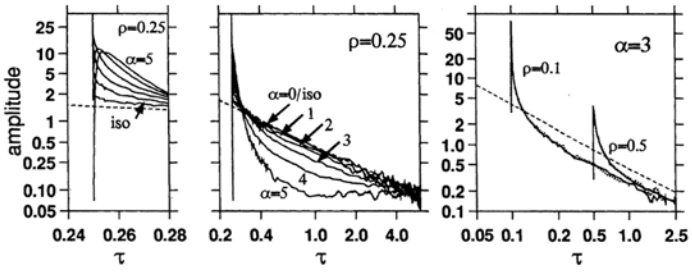

Figure 6. The near-onset (left) and the general (centre) pattern of envelopes in the 'fractal' case, for various values of the exponent α of spectral decay, with the value of the cut-off angle $\theta_0 = 6°$. On the right, the independence of the envelope shape from the θ_0 value is illustrated: the difference between the simulated curves for $\theta_0 = 3°$ (solid line) and $\theta_0 = 10°$ (dotted line) is below numerical noise. The asymptotic coda shape for the isotropic case is shown by dashes. τ step/bin size: left plot: 0.0001, middle plot: 0.0001 up to $\tau = 0.5$ and 0.04 later; right plot: 0.04.

$\rho = 0.25$, $\theta_0 = 6°$ and α values from 0 to 5. Both the general shape and the 'direct' pulse are separately presented. The envelope shapes do not perceptibly depend on the θ_0 parameter until it is small enough; only the value of α matters (therefore this is indeed the fractal case). This is illustrated by the right box of Fig. 6 where we compare envelopes, simulated for $\alpha = 3$ and $\rho = 0.1$ and 0.5, for two different values of θ_0: 3° and 10°. The modelled envelopes for these cases are seen to coincide within the modelling error. This is a clear illustration of the negligible effects of large-size inhomogeneity on real envelopes. Notice that at $\alpha \leq 4$, the deviation of the coda level from that of the isotropic case does not exceed half an order of magnitude. At $\alpha = 5$, however, this deviation becomes much larger.

Mixed Gaussian-ACF and isotropic indicatrix

This case combines very short-wavelength and long-wavelength inhomogeneity without any intermediate-wavelength inhomogeneity (compare Wu & Aki 1985a). It is interesting, at least as a certain limiting case; also, despite its intuitively not very realistic character, it provides the best qualitative fit to real data (more on this below). Fig. 7 shows the general shape of envelopes for $\rho = 0.30$ and the zoomed near-onset part for $\rho = 0.245$. We show the results for the Gaussian-ACF indicatrix ($\sigma = 6°$), with the variable admix of the isotropic indicatrix (i.e. the actual indicatrix function is the weighted average of the two, and the relative weight of the latter is the 'per cent' parameter). Again, the general picture does not depend on the choice of a particular σ value until σ is small enough. One can see that by manipulating the relative weight of the isotropic component one can produce a family of curves generally reminiscent of those for the fractal case with various α, or for the Gaussian-ACF case with various σ. One important difference from the fractal case is that the onset of the pulse is not abrupt throughout the whole range of parameters studied.

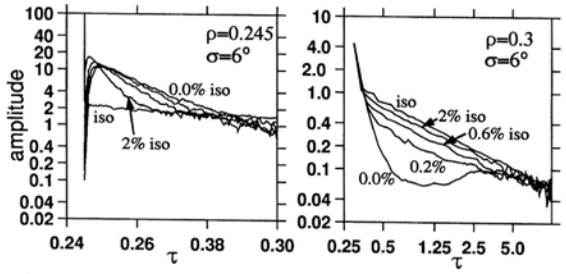

Figure 7. The near-onset and the general pattern of envelopes in the case of the mixed Gaussian-ACF ($\sigma = 6°$) and isotropic indicatrices, for 0 per cent, 0.2 per cent, 0.6 per cent, 2 per cent and 100 per cent contributions of the isotropic component τ step: left plot: 0.0001; right plot: 0.04.

PEAK DELAY OF THE 'DIRECT' WAVE PULSE

We also studied the delay of the peak of the 'direct' wave pulse with respect to the onset time, i.e. the peak delay τ_m. The results of our modelling are partly shown in Fig. 8. Four series of τ_m values are given: the Gaussian-ACF case with $\sigma = 3°$ and 20°, and the 'fractal' case with $\alpha = 3$ and 4 (at small $\theta_0 = 6°$). Plots are not fully smooth due to the combined result of numerical noise and the effects of finite bin size, but the general trends are obvious. In the case of a narrow indicatrix (Gaussian ACF, $\sigma = 3°$) over the wide range of $\rho = 0.05$ to 2, the modelled τ_m value, within our accuracy limits, coincides with the quadratic trend

$$\tau_m \approx 0.091\rho^2, \tag{23}$$

which is predicted (for $\rho \ll 1$ only), based on the relevant theory of Williamson (1972, 1975). This theory describes an energy pulse propagating from a point source through a 3-D scattering medium with Gaussian ACF at large ka (that is, small σ) (or, essentially, with any very narrow indicatrix), and its asymptotic shape is given by

$$i(\rho, \tau_1) = \frac{2\pi^2}{\rho^2} \sum_{n=1}^{\infty} (-1)^{n-1} n^2 \exp\left(\frac{-\pi^2 n^2 \tau_1}{\rho^2}\right), \tag{24}$$

where $\tau_1 = \tau - \rho$. We determined the value of the coefficient in (23) by setting the derivative of (24) to zero and solving the resulting equation numerically. The value of 0.091 obtained slightly improves our earlier Monte-Carlo result of 0.1 (Abubakirov & Gusev 1990). At $\rho > 2$–3, the modelled curve departs upwards from this trend, and begins to approach the predictions of the diffusion model (Aki & Chouet 1975), for which it is easy to show that $\tau_m = \rho^2/2 - \rho$. The curve for $\sigma = 20°$ begins at $\rho = 0.55$ because no lagged peak exists at smaller ρ. Its trend at greater distances illustrates the convergence of waveforms, mentioned above, to the asymptotic (small σ) shape represented here by the case $\sigma = 3°$.

In the 'fractal' case, the diffusion asymptote is the same, as would be expected, but deviations from the quadratic trend (7) are manifested much more clearly. A lagged peak appears

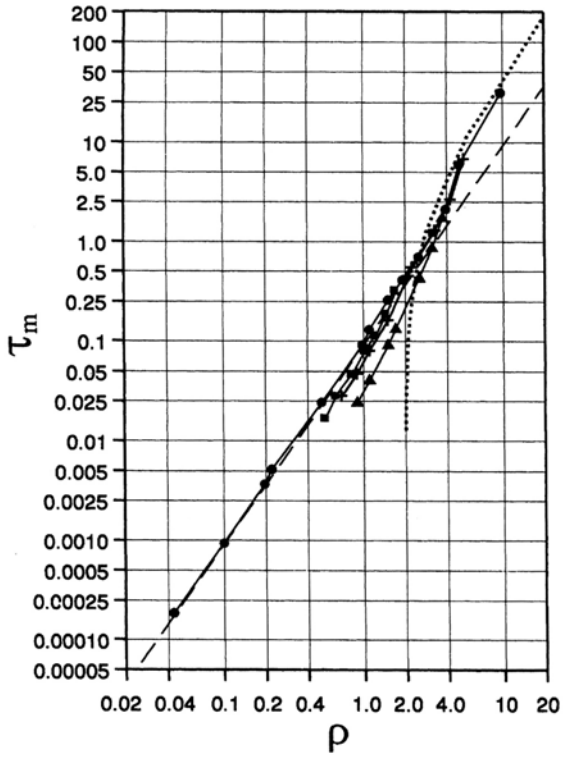

Figure 8. 'Direct-pulse' broadening with distance, expressed as onset-to-peak delay τ_m versus ρ. Symbols denote the results of simulation: two variants of the Gaussian-ACF case with $\sigma = 3°$ (dots) and 20° (squares); and two variants of the 'fractal' case with $\alpha = 3$ (triangles) and $\alpha = 4$ (crosses). Dashes show the relationship (23) derived from the Williamson (1972) analytical pulse shape; it is extrapolated well above the region $\rho \ll 1$ where this result must be valid. The formulas of Williamson (1972) were derived for the case of a narrow indicatrix, and should be compared to the Gaussian-ACF case, $\sigma = 3°$. The dotted line is the analytical result for the diffusion case and must be valid, at $\rho \gg 1$, for any indicatrix. In both (asymptotic) cases, analytical results match the results of simulation well.

at $\rho \approx 0.6$ at $\alpha = 4$ and only at $\rho \approx 0.9$ at $\alpha = 3$. In this last case, deviations from the Gaussian case persist up to $\rho = 3$. Numerically, the difference is as great as 3 times at $\rho = 1$ for $\alpha = 3$. One observes that the dimensionless distance where the lagged peak arises is closely related to the indicatrix type; the value of τ_m at $\rho = 1$ is also informative. It is worth remembering that for the isotropic case there is no peak delay at all: the theoretical pulse onset is always abrupt and delta-like (see Fig. 4); it is, however, hardly observable at $\rho > 3$–4.

Note that the deviations of τ_m from those for the case of Gaussian ACF with a narrow indicatrix are, in all cases studied, of the same negative sign. This strongly suggests that this case can play a specific role in providing the upper boundary for τ_m (and other pulse duration measures as well).

QUALITATIVE COMPARISON OF MODELLED AND REAL ENVELOPES

We can now compare the properties of the modelled envelopes with those of the observed ones. As we have already mentioned, the two most obvious properties of the observed envelopes are the monotonous 'qualitatively isotropic' coda shape and the broadening of the 'direct' wave pulse with distance. As an illustration, Fig. 9 is a reproduction of Fig. 7 from Rautian & Khalturin (1978). One can see that there is a well-defined asymptotic envelope shape, or coda, and that individual envelopes approach this coda shape monotonously and, in general, from above. This picture qualitatively corresponds to the isotropic scattering case (Fig. 4) for $\rho \leq 1$. Such an analogy was seemingly the main reason why the single isotropic scattering model was so widely applied to data interpretation. We emphasize that this behaviour is very typical, and can be observed simultaneously for several bands over a very wide frequency range. As we consider only body waves here, we can speak with confidence about the 1 to 40 Hz range, which covers more than 1.5 decades. To illustrate the pulse broadening we reproduce in Fig. 10 Fig. 4 from Sato (1989). Here one can see the pulse broadening with distance simultaneously in five adjacent frequency bands covering the same frequency range.

One more observational constraint is the frequency dependence of the 'observed' mean free path, which we denote l. The observed l versus f trends range from $\approx f^{-1}$ (Rautian *et al.* 1981) through $\approx f^{-1/2-0}$ (Wu & Aki 1985b; Gusev & Lemzikov 1983, 1985) to $\approx f^{1/2}$ (Hoshiba 1993; Mayeda *et al.* 1992). Generally speaking, the most intensive scattering takes place

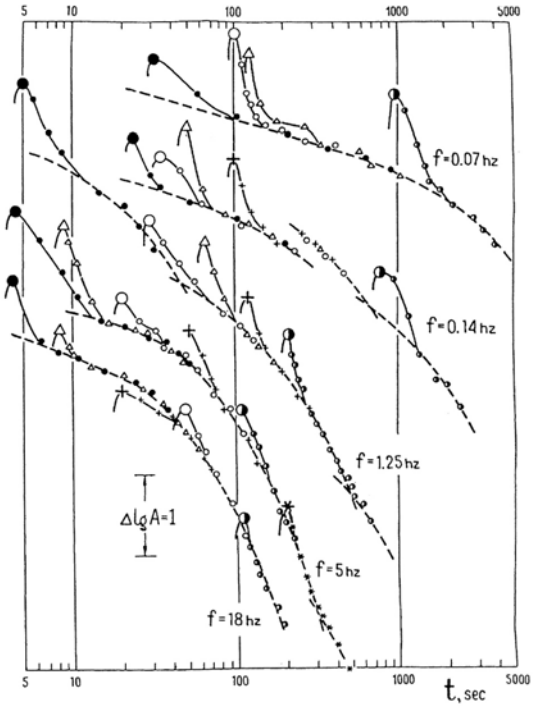

Figure 9. Observed envelopes for five frequency bands (symbols) and asymptotic coda shapes approximated by a sequence of dashed curves. The observed envelopes are scaled arbitrarily for the sake of presentation. Only the lower three plots can be thought to result from body-wave (3-D) scattering. Station Garm, Tajikistan. Reproduced from Rautian & Khalturin (1978) with permission of the Seismological Society of America.

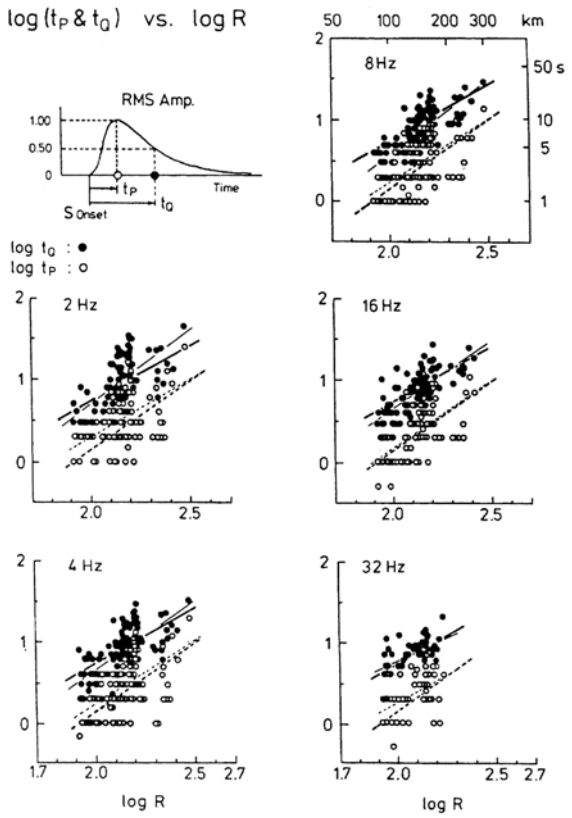

Figure 10. Onset-to-peak t_P (circles) and onset-to-the-later-half-peak t_Q (dots) delay times versus hypocentral distance, for small earthquake *S* waves propagating through the uppermost mantle for five frequency bands. Thicker lines show the linear regression; their slopes are somewhat below the theoretical value of 2. Station Ashio, Japan. Reproduced from Sato (1989), copyright held by the American Geophysical Union.

when the wavelengths of inhomogeneity and of wavefield match (ka is of the order of unity), as was formally shown e.g. for elastic backscattering by Wu & Aki (1985a). Hence, if, following Wu & Aki (1985b), we assume the inhomogeneity field to be self-affine (fractal) in the relevant wavenumber range, the listed trends imply the corresponding trends for the inhomogeneity spectrum: it must have a power-law behaviour ($k^{-\alpha}$), with the α values in the range 3–4.5, i.e. either the inhomogeneity is self-similar [k^{-3}; $Q^{-1}_{\text{scatter}}(f) = \text{const}$] or it is somewhat 'redder', i.e. the absolute value of α is in excess of 3 (see Wu & Aki 1985b for details).

Let us now correlate this observational evidence with our modelled envelopes. Putting aside the 'mix' model as less probable, we note that a qualitatively acceptable fit can be attained by the Gaussian-ACF model with $\sigma = 30°$–$40°$, and by the 'fractal' model with $\alpha = 3$–4: at this choice of parameters, both produce pulse broadening and at the same time monotonously decaying codas. At $\sigma = 20°$ or $\alpha = 5$, one can see constant-amplitude codas that have never been reported. At $\sigma = 60°$ or $\alpha = 2$, 'direct pulses' are delta-like up to $\rho = 1$–2: this means that one would be able to observe body-wave pulses with a source-related duration at distances of 100–200 km, which again does not agree with observations. We can thus bracket the reasonable range of parameters for the two compared models.

In order to discriminate between the two models, one can employ the fact that they behave in a radically different way over a wide frequency range. To see this, imagine a typical data processing set-up with several frequency bands independently analysed, with octave bands, and band central frequencies in geometric progression as (1, 2, 4, ...). Assume that we have fitted data of some particular band with the central frequency $f = f_1$ by the theoretical envelope for the Gaussian ACF with $\sigma = 40°$. Now note that the parameter σ is in fact frequency–dependent: $\sigma = 1.41/ka = \text{const}/f$, so if we have correctly fitted $\sigma = 40°$ in a band with a particular value of central frequency (f_1), σ must take different values for other bands, with other central frequencies. For example, for the 'neighbouring' frequency bands with central frequencies $f_1/2$ and $2f_1$, the value of σ will be equal to 80° and 20°, respectively. Therefore, following the Gaussian-ACF model, we would expect in the lower ($f_1/2$) band a lack of pulse broadening and a short ('source') pulse up to distances of 100 km and more, and in the higher ($2f_1$) band up to 40–50 km hypocentral distance, a very fast decay of early coda, just after arrival, and then an almost constant coda level during the next 40 s. Both predictions are inconsistent with the data, which show qualitatively similar envelopes for any frequency band within the 0.3–30 Hz range. (This qualitative pattern alone strongly suggests the fractal character of inhomogeneity).

With the fractal model, the situation is different: its only critical parameter, α, is unrelated to frequency. The other parameter, θ_0, has been shown above to be irrelevant if small enough, and we will assume this. Such an assumption means that the low-wavenumber boundary of the 'fractal' behaviour of the inhomogeneity field is much lower than the wavenumber of the wavefield under question. Being frequency-independent, α can be fitted simultaneously over a wide frequency range. Therefore, the fractal model fares much better, and we consider it as the preferred one.

We now note a very remarkable fact, namely that the 'observed' α range from sources listed in the second paragraph of this section, 3–4.5, roughly coincides with the α range where the qualitative observational constraints (monotonous coda and pulse broadening) more or less agree with our modelled envelopes. However, these constraints are best met in a somewhat narrower range. Indeed, at $\alpha = 3$, non-zero peak delay appears only at $\rho \approx 0.9$ which seems too far, and at $\alpha > 4$, coda shape deviation from the isotropic case seems too large to be acceptable. Therefore, in terms of the 'fractal' model, its probable parameter can be put within the rather narrower brackets of $\alpha = 3.5$–4.

However, even for optimal combinations of parameters, the quality of the fit of the modelled envelopes is marginal in the Gaussian-ACF case. Indeed, no really good compromise can be seen in Fig. 4: the delta-like true direct wave still exists even for $\sigma = 20°$, $\rho = 0.245$, although much reduced, whereas coda decay is already too fast. The fit is not very good in the 'fractal' case either, where for quite acceptable coda, for $\alpha = 3$, the abrupt character of the pulse leading edge disappears at $\rho = 0.9$, i.e. evidently too late, whereas for $\alpha = 4$, coda decay seems too fast, and the interval where the leading edge is abrupt is still too wide (up to $\rho = 0.6$). Curiously enough, the

'mix' model gives the best qualitative fit: at the isotropic admix value of 2 per cent, delta-like onset is suppressed even at $\rho = 0.25$, whereas the difference between corresponding coda and 'isotropic' coda is rather small (Fig. 7). However, we are not inclined to ascribe physical meaning to this result, because the 'mix' model does not seem to be a plausible one for the inhomogeneity structure of the real Earth. There are other ways to improve the limited success of the fractal model, primarily by taking into account the strong vertical non-uniformity of scatterer density (Gusev 1995).

A reasonable fit of observed envelopes by three particular inhomogeneous models, each with its own parametrization, suggests that it may be possible to introduce a single general parameter relating indicatrix shape to the shapes of the corresponding envelope family. The simplest idea is to use the l_e to l_n ratio (or $\langle \cos\theta \rangle$). The numerical values of $\beta = l_e/l_n$ that correspond to an acceptable fit in fact cover rather a wide interval. Consider numerical values of β that correspond to the values of model parameters that bracket the acceptable fit. For the Gaussian-ACF model, for $\sigma = 20°$ (40°), $\beta = 8.2$ (2.2); for the 'fractal' model, for $\alpha = 4$ (3), $\beta = 8.7$ (2.4), which is comparable. However, for the 'mix' model (at $\sigma = 6°$), for a fraction of isotropic component equal to 2 per cent, $\beta = 32$ (we prefer a point estimate here instead of the interval). One possible cause of such a difference is that despite the fact that the probability of backscatter ($\theta > 90°$) is much higher in the last case, this fact does not manifest itself clearly in the calculation of $\langle \cos\theta \rangle$. Nevertheless, it seems that the value of $\beta = l_e/l_n$ may serve as a rough description of the 'forward-enhanced' property of an indicatrix. The search for a more adequate parameter is an interesting problem for further study.

DISCUSSION

The multiscale ('fractal') scattering inhomogeneity structure was briefly discussed by Gusev & Lemzikov (1983, 1985) and in more detail by Wu & Aki (1985b). In both studies, a 'red' self-affine structure, with the enhanced large-wavelength part of the wavenumber spectrum, was deduced from the observational data on *S* waves and coda from near earthquakes. Sato (1990) (expanding on Sato 1982) considered the Von Karman inhomogeneity spectrum (it has a power-law high-frequency tail producing fractal-like behaviour at high frequencies), and, having combined various techniques, obtained the rather definite estimate of 0.35 for the 'order' parameter of the Von Karman spectrum; in terms of the power-law behaviour, this means $\alpha = 3.7$. From the data on pulse broadening in the mantle under Ashio station (Sato 1989; Sherbaum & Sato 1991), an α value of 4 could be fairly reliably deduced. However, Obara & Sato (1995) found parameters of broadening to vary over different mantle volumes, and their data indicate a range of α from 3 to 4 for different volumes. Based on array observations of 2 Hz teleseismic *P*, Flatté & Wu (1988) arrived at the comparable model of the scattering lithosphere, which consists of two overlapping layers with $\alpha = 0$ (depth range 0–200 km), and $\alpha = 4$ (depth range 15–250 km). We have been able to show here that the 'red' self-affine model (with $\alpha =$ 3.5–4) is in qualitative agreement with the features of observed *S*-wave envelopes. This estimate is in excellent agreement with Sato's (1990) estimate of 3.7. Note that the α value can (and does, see Obara & Sato 1995) vary for different Earth subvolumes; thus it does not seem meaningful to try to find a point estimate for the whole lithosphere. We believe that at present the fractal model with $\alpha = 3.5$–4 can be considered as a good reference one, or as a starting approximation in detailed studies.

A tradition in scattering studies is to describe the degree of scattering by the scattering coefficient α_s or by its inverse, l_n. Although these parameters are fully adequate in a theoretical study, we note that from the point of view of interpretation of data, l_e seems the better candidate as a single parameter: in the simplest Gaussian-ACF case, it alone defines two measurable properties of the scattered envelope: the pulse broadening rate and the late coda level. If the value of $\beta = l_e/l_n$ can also be estimated from the data (and this seems typically a much more difficult task), the l_e–β combination may provide a compact description of data. (Our own brackets for β are clearly too wide: 2.5–30). In this case, an observational estimate of l_n ($= l_e/\beta$) can also be found.

CONCLUSION

We have simulated scattered body-wave envelopes predicted by models of the lithospheric inhomogeneity and qualitatively compared the results with the observed patterns. We found that whereas the Gaussian autocorrelation model is capable of reproducing observed features reasonably well in any particular frequency band, it fails to describe observations in the wide frequency range. An inhomogeneity structure which is near to a self-affine fractal one seems to be much more likely. Its wavenumber spectrum must be, approximately, a power-law one, with an exponent value of around 3.5–4.

ACKNOWLEDGMENTS

This study was supported financially by the Russian Foundation for Fundamental Research, RFFI grant No. 93-05-8514. H. Sato kindly provided preprints of his papers. The authors are indebted to two anonymous reviewers for useful comments.

REFERENCES

Abubakirov, I.R. & Gusev, A.A., 1990. Estimation of scattering properties of lithosphere of Kamchatka based on Monte-Carlo simulation of record envelope of a near earthquake, *Phys. Earth. planet Inter.*, **64,** 52–67.

Aki, K., 1969. Analysis of the seismic coda of local earthquakes as scattered waves, *J. geophys. Res.*, **74,** 615–631.

Aki, K. & Chouet, B., 1975. Origin of coda waves: source, attenuation and scattering effects, *J. geophys. Res.*, **80,** 3322–3342.

Flatté, S.M. & Wu, R.S., 1988. Small-scale structure in the lithosphere and astenosphere deduced from arrival time and amplitude fluctuations at NORSAR, *J. geophys. Res.*, **93,** 6601–6614.

Gusev, A.A., 1995. Vertical profile of turbidity and coda Q, *Geophys. J. Int.*, **123,** 665–672.

Gusev, A.A. & Abubakirov, I.R., 1987. Monte-Carlo simulation of record envelope of a near earthquake, *Phys. Earth. planet Inter.*, **49,** 30–36.

Gusev, A.A. & Lemzikov, V.K., 1983. Estimation of scattering parameters of shear waves in the crust and upper mantle of Kamchatka according to observations of 'Shipunski' station, *Vulkanol. Seismol.* No. 1, 94–108.

Gusev, A.A. & Lemzikov, V.K., 1985. Properties of scattered elastic waves in the lithosphere of Kamchatka: parameters and temporal variations, *Tectonophysics,* **112,** 137–153.

Hoshiba, M., 1993. Separation of scattering attenuation and intrinsic

absorption in Japan using the multiple lapse time window analysis of full seismogram envelope, *J. geophys. Res.,* **98,** 15 809–15 824.

Hoshiba, M., 1995. Estimation of non-isotropic scattering in western Japan using coda wave envelopes: application of a multiple non-isotropic scattering model, *J. geophys. Res.,* **100,** 645–657.

Ishimaru, A., 1978. *Wave Propagation and Scattering in Random Media,* Vols 1 & 2, Academic, San Diego, CA.

Mayeda, K., Koyanagi, S., Hoshiba, M., Aki, K. & Zeng, Y., 1992. A comparative study of scattering, intrinsic and coda Q^{-1} for Hawaii, Long Valley and Central California between 1.5 and 15 Hz, *J. geophys. Res.,* **97,** 6643–6659.

Obara, K. & Sato, H., 1995. Regional differences of random inhomogeneities around the volcanic front in the Kanto–Tokai area, Japan, revealed from the broadening of S wave seismogram envelopes, *J. geophys. Res.,* **100,** 2103–2122.

Rautian, T.G. & Khalturin, V.I., 1978. The use of coda for determination of the earthquake source spectrum, *Bull. seism. Soc. Am.,* **68,** 923–948.

Rautian, T.G. *et al.,* 1981. *Experimental Studies of Seismic Coda.* Nauka, Moscow.

Rytov, S.M., Kravtsov, Yu.A. & Tatarskii, V.I., 1978. *Vvedenie v statisticheskuyu radiofiziku, II. Sluchainye polya,* Nauka, Moscow (in Russian); English edition: *Introduction to statistical radiophysics,* Vols 1–4, Springer, New York, 1987.

Sato, H., 1977. Energy propagation including scattering effects: single isotropic scattering approximation, *J. Phys. Earth,* **25,** 27–41.

Sato, H., 1982. Attenuation of S waves in the lithosphere due to scattering by its random velocity structure, *J. geophys. Res.,* **87,** 7779–7785.

Sato, H., 1984. Attenuation and envelope formation of three component seismograms of small local earthquakes in randomly inhomogeneous lithosphere, *J. geophys. Res.,* **89,** 1221–1241.

Sato, H., 1989. Broadening of seismogram envelopes in the random inhomogeneous lithosphere based on the parabolic approximation: Southeastern Honshu, Japan, *J. geophys. Res.,* **94,** 17 735–17 747.

Sato, H., 1990. Unified approach to amplitude attenuation and coda excitation in the randomly inhomogeneous lithosphere, *Pure appl. Geophys.,* **132,** 93–119.

Sato, H., 1995. Formulation of the multiple non-isotropic scattering process in 3-D space on the basis of the energy transport theory, *Geophys. J. Int.,* **121,** 523–531.

Scherbaum, F. & Sato, H., 1991. Inversion of full seismogram envelopes based on the parabolic approximation: estimation of randomness and attenuation in Southeast Honshu, Japan, *J. geophys. Res.,* **96,** 2223–2232.

Wesley, M.P., 1965. Diffusion of seismic energy in the near range, *J. geophys. Res.,* **70,** 5099–5106.

Williamson, I.P., 1972. Pulse broadening due to multiple scattering in the interstellar medium, *Mon. Not. R. astr. Soc.,* **157,** 55–71.

Williamson, I.P., 1975. The broadening of pulses due to multipath propagation of radiation, *Proc. R. Soc. Lond.,* A, **343,** 131–147.

Wu, R.-S., 1985. Multiple scattering and energy transfer of seismic waves—separation of scattering effect from intrinsic attenuation—I. Theoretical modelling, *Geophys. J. R. astr. Soc.,* **82,** 57–80.

Wu, R.-S. & Aki, K., 1985a. Elastic wave scattering by a random medium and the small-scale inhomogeneities in the lithosphere, *J. geophys. Res.,* **90,** 10 261–10 273.

Wu, R.-S. & Aki, K., 1985b. The fractal nature of the inhomogeneities in the lithosphere evidenced from seismic wave scattering, *Pure appl. Geophys.,* **123,** 805–818.

Zeng, Y., Su, F. & Aki, K., 1991. Scattering wave energy propagation in a random isotropic scattering medium. 1. Theory, *J. geophys. Res.,* **96,** 607–619.